Supporting Information

Friction-Assisted Electrochemical Oxidation of Iridium Surfaces for Enhanced Catalysis

Chenxu Liu[#]*, Johannes L. Hörmann[#], Haoran Pan[#], Hantao Xu, Lianhuan Han, Jun Cheng, Xingxing Chen*, Hongbo Zeng*, Yonggang Meng*, Yu Tian*

*Corresponding author. Email: mengyg@tsinghua.edu.cn, tianyu@mail.tsinghua.edu.cn, hongbo.zeng@ualberta.ca, xingchenstar@ustl.edu.cn, liuchenxu19910407@163.com.

This PDF file includes:

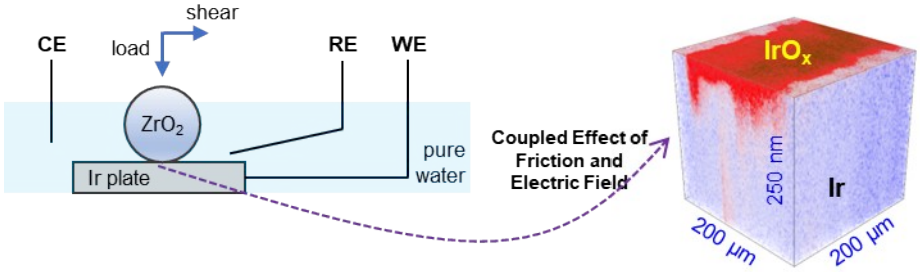

Fig. S1. Schematic illustration of the setup for friction-assisted localized electrochemical oxidation of Ir and the resulting IrO_x formed on the Ir surface measured by TOF-SIMS.

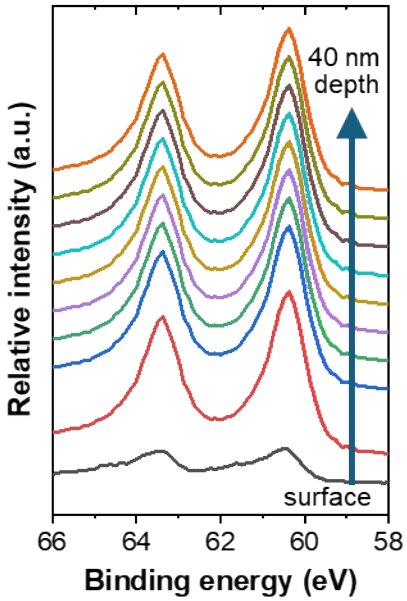

Fig. S2. XPS spectra of the Ir 4f of the IrO_x layer recorded as sputtering depth increases. Sampling area: 50×50 μm; sputtering depth: 4.44 nm per interval.

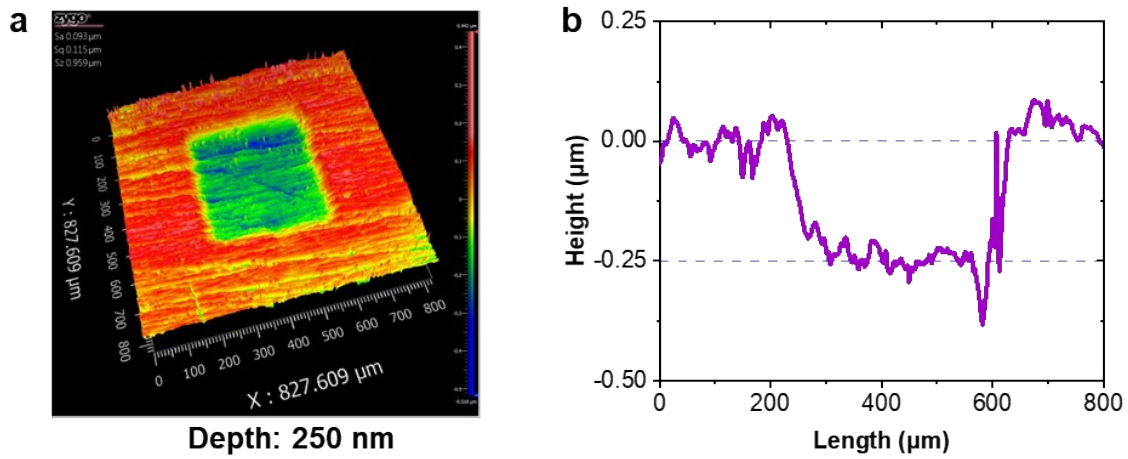

Fig. S3. 3D morphology (a) and profile (b) of the wear track on Ir plate surface, after the ToF-SIMS measurement. The splash time was 1200 s, and the sputtering depth measured by a 3D optical profiling instrument (ZYGO NexView, USA) was about 250 nm.

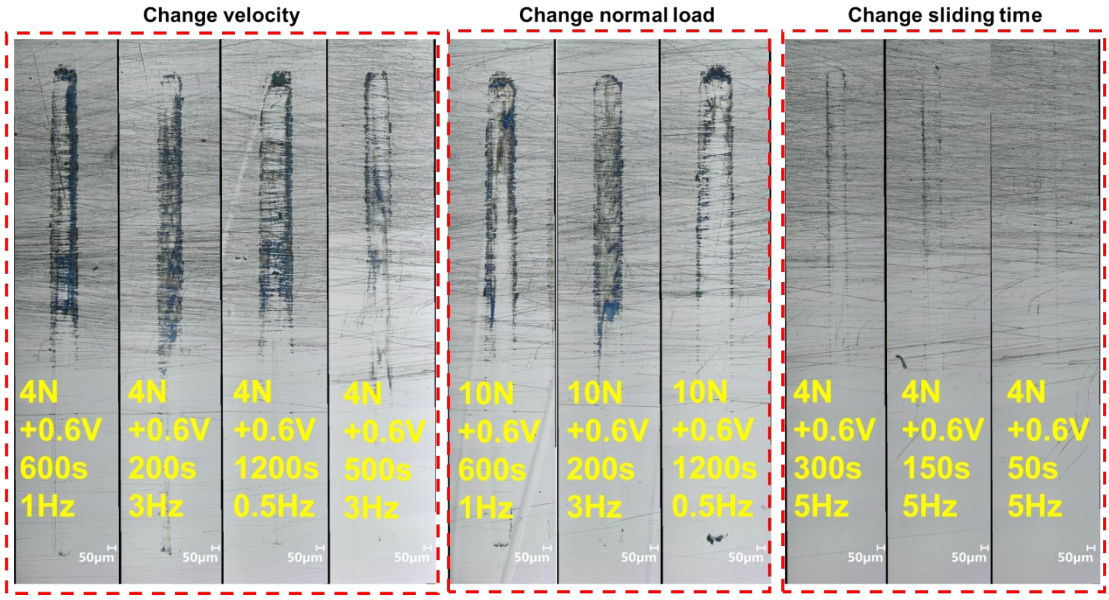

Fig. S4. Effect of velocity, normal load and sliding time on the formation of IrO_x on Ir surface. The parameters of the friction experiment are marked in the figure.

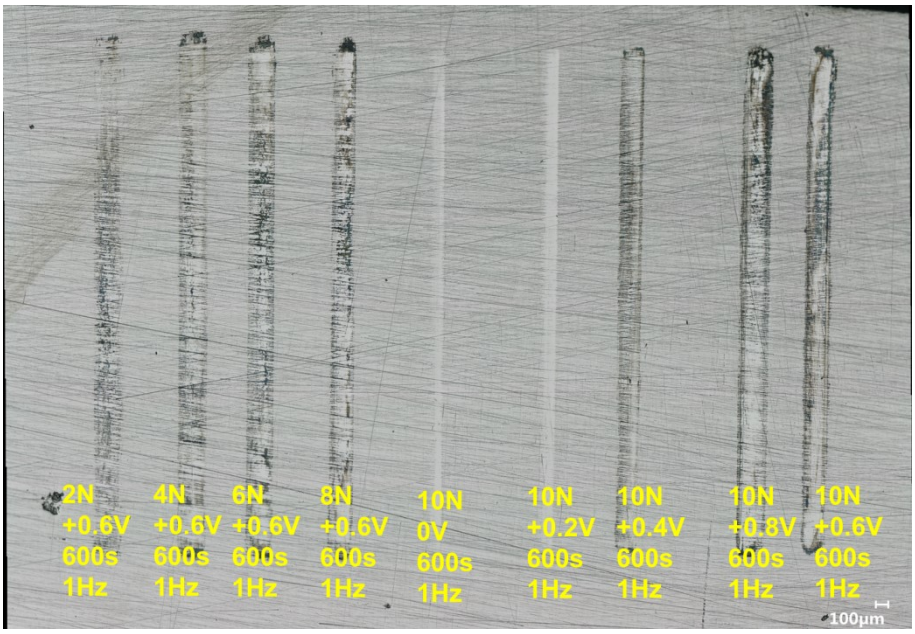

Fig. S5. Effect of surface potential on the formation of IrO_x on Ir surface. The parameters of the friction experiment are marked in the figure.

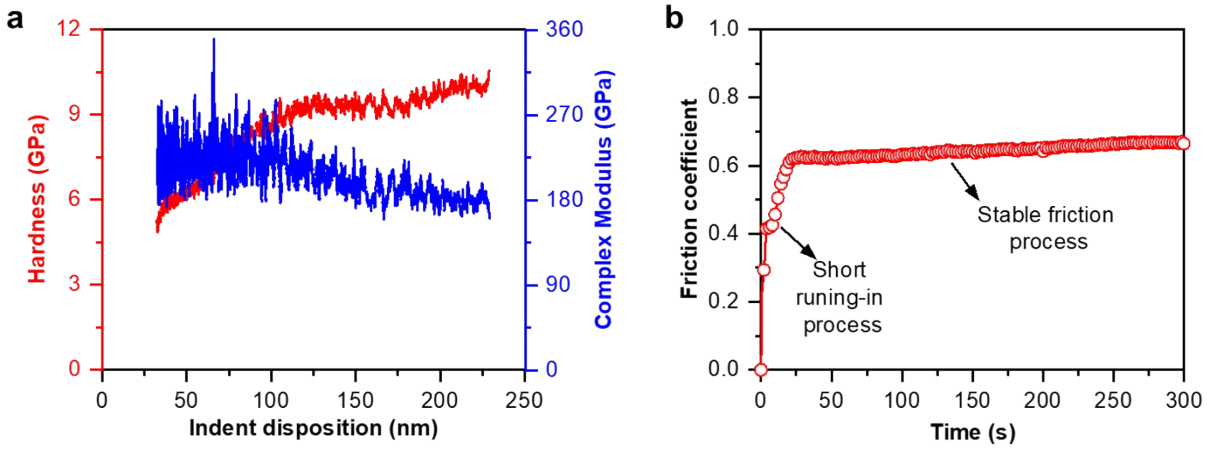

Fig. S6. Mechanical properties of the friction-assisted electrochemical IrO_x layer. (a) Depth-dependent hardness and complex modulus; (b) Variation of the friction coefficient between the oxide layer and ZrO_2 ball (with a diameter of 6.35 mm, under 4 N) over time.

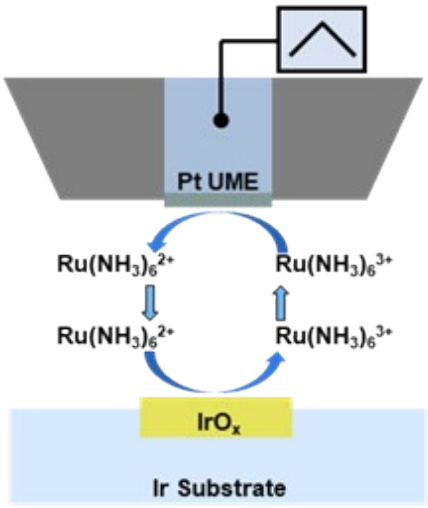

Fig. S7. The diagram of the scanning electrochemical microscopy for the electrochemical activity measurement of Ir and IrO_x mixture. The electrolyte contains 1 mM $Ru(NH_3)_6Cl_3$ and 0.1 M K_2SO_4. The motion rate of Pt UME was set as 20 μm/s. The UME-substrate distance was kept constant at 4 μm.

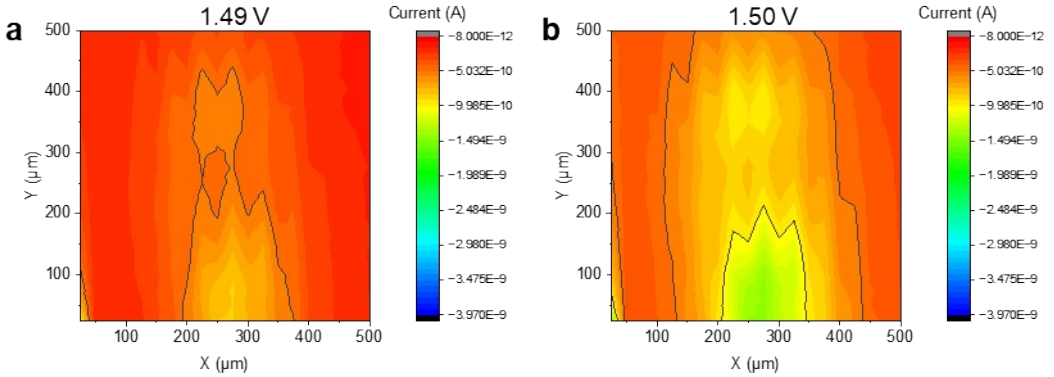

Fig. S8. OER activity distribution on the surface of Ir-IrO_x at potentials of (a) 1.49 V_{RHE} and (b) 1.50 V_{RHE}. The Pt-tip substrate distance was kept constant at 15 μm.

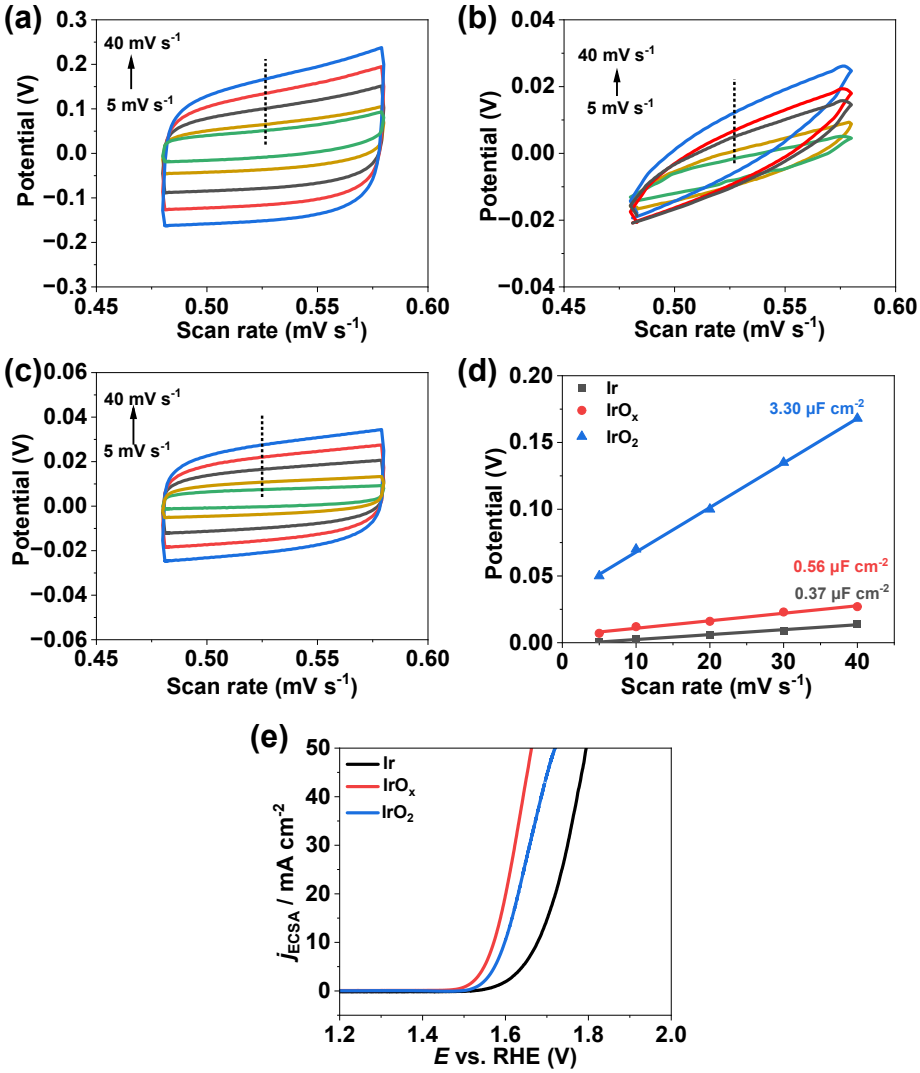

Fig. S9. (a-c) CV curves at different scan rates (5~40 mV s^{-1}) for IrO_2, Ir and IrO_x. (d) Electrochemical double-layer capacitance. (e) OER activity comparison of IrO_2, Ir and IrO_x using ECSA-based analysis.

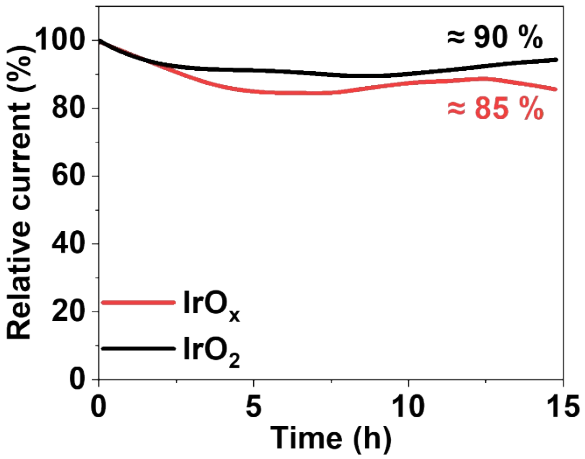

Fig. S10. Chronopotentiometry of OER at constant potential of 1.65 V.

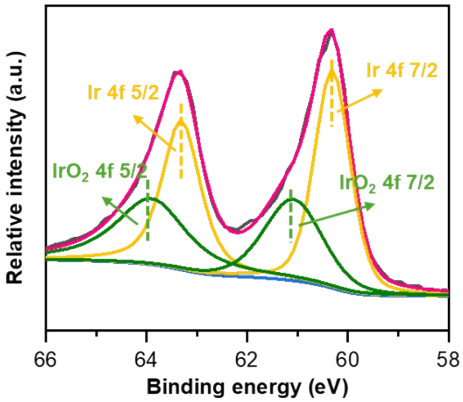

Fig. S11. XPS spectrum of the Ir 4f of the original wear surface on the lower friction pair after the OER measurements.

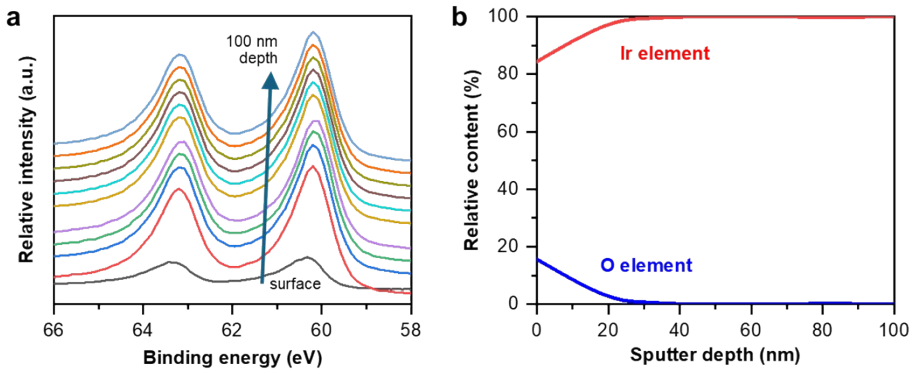

Fig. S12. XPS spectra of the Ir 4f of the IrO_x layer after the OER measurements recorded as sputtering depth increases. (a) Ir 4f XPS spectra at different sputtering depths; (b) relative atomic contents of Ir and O as a function of sputtering depth. Sampling area: 50×50 μm; sputtering depth: 10 nm per interval.

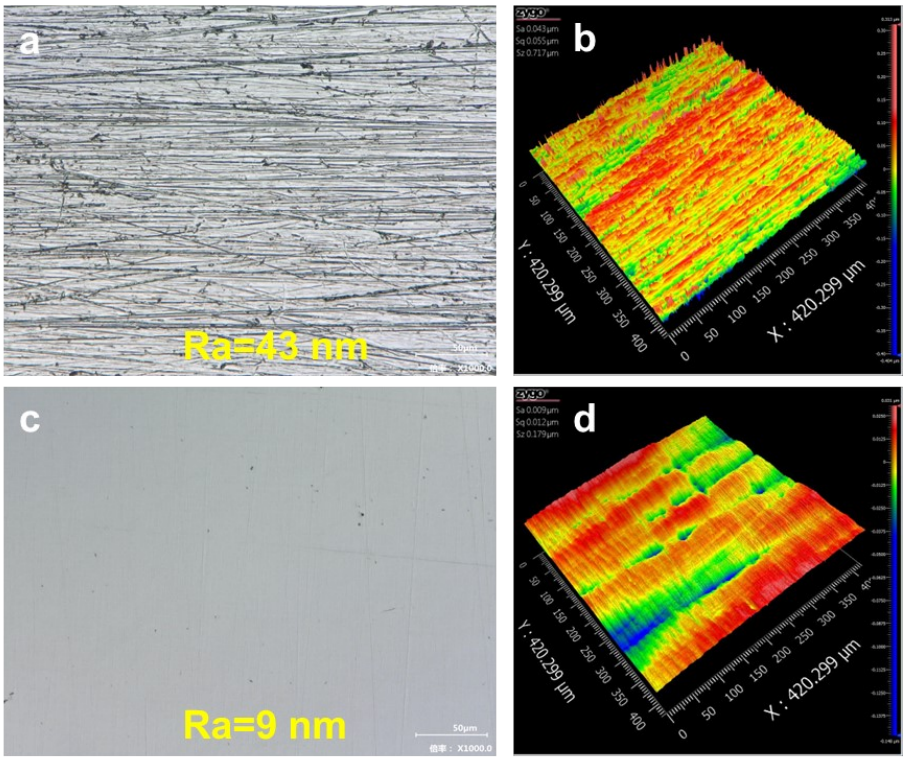

Fig. S13. Microscopic morphologies of rough and smooth Ir metal surfaces before performing any friction test. Optical microstructure (a) and 3D morphology (b) of rough surface; Optical microstructure (c) and 3D morphology (d) of smooth surface.

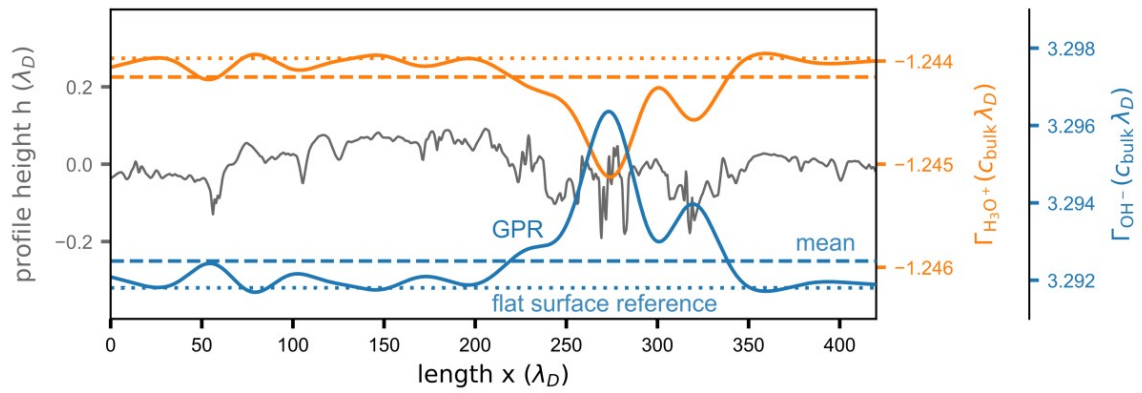

Fig. S14. Effect of surface potential on the formation of IrO_x on Ir surface. The parameters of the friction experiment are marked in the figure. Delocalized surface excess trends smeared out to larger length scales by Gaussian process regression (GPR) from data in Figure.3D. Dotted lines show the reference surface excess for an ideally flat surface. Dashed lines show the mean surface excess over the whole line scan. The Debye length λ_D serves as the spatial unit. Surface excess Γ is measured in units of $c_{bulk} \cdot \lambda_D$. In water of pH 7, $\lambda_D \approx 1\,\mu m$ and $c_{bulk} = 10^{-4}\,mol\,m^{-3}$ for both hydronium and hydroxide. A kernel of two summed radial basis functions with the initial hyperparameters length scale 10 and 50 and variance 0.01 for both has been used to perform GPR on the dimensionless data in Figure.3D.

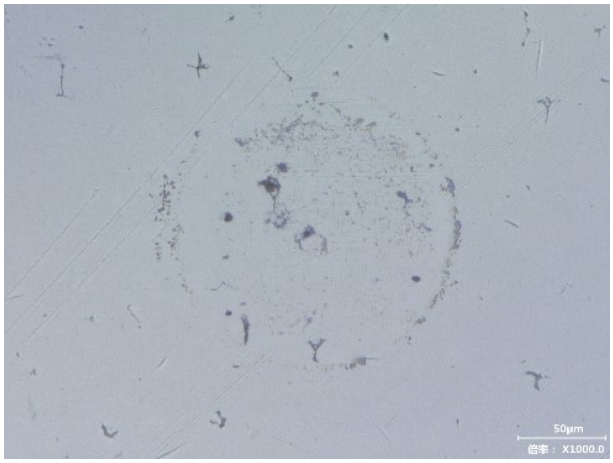

Fig. S15. Surface morphologies of the ZrO_2 ball after the friction test of 200 s with pure water as lubricant under a positive surface potential of +0.6 V (Ag/AgCl as the reference electrode).

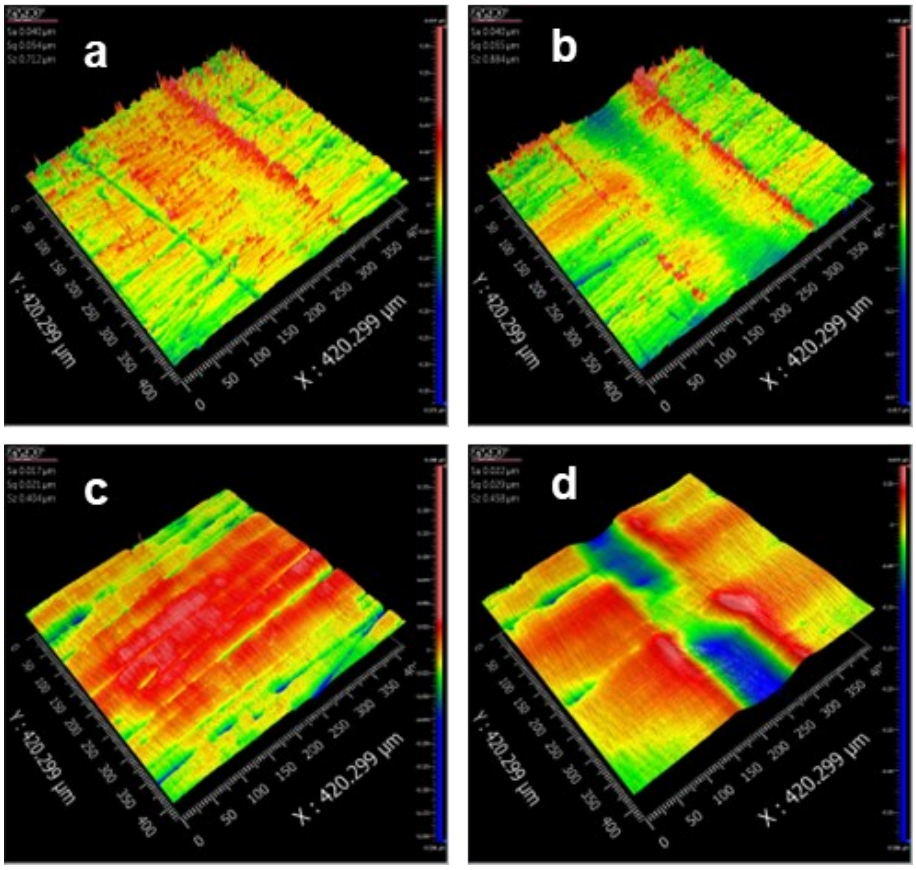

Fig. S16. 3D morphologies of wear tracks on Ir plates with varying surface roughness under different normal loads. (a) and (b) show wear tracks on smooth and rough surfaces after friction tests at a 4 N load (1.18 GPa); (c) and (d) show wear tracks on smooth and rough surfaces after tests at a 10 N load (1.62 GPa). All tests were conducted at a surface potential of +0.6 V, a frequency of 3 Hz, and a duration of 200 s.

Table S1. Comparison of the overpotential at 10 mA cm^{-2}: the friction-induced amorphous IrO_x layer in this work vs. recently reported amorphous Ir or IrO_x-based catalysts.

Catalyst	Electrolyte	Overpotential	Reference
IrO_x	0.1 M $HClO_4$	310	This work
Commercial IrO_2	0.1 M $HClO_4$	386	[1]
Amorphous Ir NSs	0.1 M $HClO_4$	255	[2]
IrO_x/TiN NPs	0.1 M $HClO_4$	293	[3]
IrO_x/TiO_2	0.1 M $HClO_4$	255	[4]
Pd@Ir	0.1 M $HClO_4$	300	[5]
Ir-MnO_2	0.1 M $HClO_4$	288	[6]
5% Nd-IrO_x	0.1 M $HClO_4$	254	[7]
$IrIrO_xH_ySe_z$/H CC	0.5 M H_2SO_4	308	[8]
$IrNiO_x/WO_3$	0.5 M H_2SO_4	239	[9]
$RuIrO_x$	0.5 M H_2SO_4	233	[10]

Supplementary references:

1. M. Sun, H. Huang, X. Niu, et al., "Grain boundary-derived local amorphization enhances acidic OER," *ACS Catalysis* 14 (2024): 15764. https://dx.doi.org/10.1021/acscatal.4c03746.
2. G. Wu, X. Zheng, P. Cui, et al., "A general synthesis approach for amorphous noble metal nanosheets," *Nature Communications* 10 (2019): 4855. https://dx.doi.org/10.1038/s41467-019-12859-2.
3. X. Han, T. Mou, A. Islam, et al., "Theoretical prediction and experimental verification of IrO_x supported on titanium nitride for acidic oxygen evolution reaction," *Journal of the American Chemical Society* 146 (2024): 16499. https://dx.doi.org/10.1021/jacs.4c02936.
4. G. Yu, R. Li, Y. Hu, et al., "Supporting IrO_x nanosheets on hollow TiO_2 for highly efficient acidic water splitting," *Nano Research* 17 (2024): 6903. https://dx.doi.org/10.1007/s12274-024-6681-7.
5. F. Xue, X. Guo, B. Min, et al., "Unconventional high-index facet of iridium boosts oxygen evolution reaction: how the facet matters," *ACS Catalysis* 11 (2021): 8239. https://dx.doi.org/10.1021/acscatal.1c01867.
6. W. Sun, Z. Wang, X. Tian, et al., "In situ formation of grain boundaries on a supported hybrid to boost water oxidation activity of iridium oxide," *Nanoscale* 13 (2021): 13845. https://dx.doi.org/10.1039/D1NR01795K.
7. G. Liu, L. Chen, Z. Liu, et al., "Short-range-engineered Nd-doped IrO_x enables oxide path mechanism for high-performance PEM water electrolysis," *Small* e11956. https://dx.doi.org/https://doi.org/10.1002/smll.202511956.
8. M.-G. Kim, H. J. Lee, T. K. Lee, et al., "Iridium selenium oxyhydroxide shell for polymer electrolyte membrane water electrolyzer with low ir loading," *ACS Energy Letters* 9 (2024): 2876. https://dx.doi.org/10.1021/acsenergylett.4c00884.
9. H. Zhang, P. Song, X. Mei, et al., "Amorphous-crystalline interface coupling of $IrNiO_x/WO_3$ for efficient and stable acidic water splitting," *ACS Catalysis* 15 (2025): 12395. https://dx.doi.org/10.1021/acscatal.5c02782.

10. Z. Zhuang, Y. Wang, C.-Q. Xu, et al., "Three-dimensional open nano-netcage electrocatalysts for efficient pH-universal overall water splitting," *Nature Communications* 10 (2019): 4875. https://dx.doi.org/10.1038/s41467-019-12885-0.